Energy & Environmental Science

ROYAL SOCIETY OF CHEMISTRY

COMMUNICATION

View Article Online
View Journal | View Issue

Check for updates

Cite this: *Energy Environ. Sci.*, 2022, **15**, 4038

Received 22nd December 2021,
Accepted 9th August 2022

DOI: 10.1039/d1ee03975j

rsc.li/ees

Reactivation of chromia poisoned oxygen exchange kinetics in mixed conducting solid oxide fuel cell electrodes by serial infiltration of lithia†

Han Gil Seo, ‡[a] Anna Staerz, ‡[a] Dennis S. Kim, [a] Dino Klotz, [ab] Clement Nicollet, [c] Michael Xu,[a] James M. LeBeau[a] and Harry L. Tuller *[a]

Solid oxide fuel cells have the potential to render the conversion from fuel to electrical energy more efficienct while lowering emissions. The technology, however, suffers from performance degradation due to cathode poisoning by chromia from metal interconnects. We confirm the deleterious impact of chromia on the performance of the model mixed conducting cathode material $Pr_{0.1}Ce_{0.9}O_{2-\delta}$ by examining the oxygen exchange coefficient (k_{chem}) *via* electrical conductivity relaxation measurements, and the area-specific resistance (ASR) by electrochemical impedance spectroscopy. Liquid Cr-infiltration decreases k_{chem} 20-fold and the oxygen exchange component of ASR increases 20-fold while maintaining the same activation energy. We then demonstrate the ability to not only recover initial k_{chem} and ASR values, but improve properties above those exhibited by the pristine specimen through subsequent Li-infiltration, leading to enhancement of k_{chem} by more than three orders of magnitude and reduction in oxygen exchange component of the ASR by over a factor 100. We attribute these dramatic changes to the depletion of electrons induced by the acidic Cr-infiltrant on the $Pr_{0.1}Ce_{0.9}O_{2-\delta}$ surface and the recovery to accumulation of electrons from the basic Li-infiltrant. These results point to acidity as a key descriptor in addressing the long-standing challenge of reactive surface poisoning in applications reliant on rapid oxygen exchange and recovery behavior. The ability to achieve remarkable levels of recovery of electrocatalytic surfaces by controlling the relative acidity of surface species is demonstrated for the first time.

Broader context

Metal oxides are an important class of functional materials for a wide array of applications, ranging from energy storage and conversion and catalysis to sensors. In many of these cases, the reaction of oxygen with the metal oxide surface plays a central role. A great deal of effort is invested in optimizing the metal oxide's initial performance. Nevertheless, the commercial viability of such devices is often markedly depressed as a result of unacceptable performance degradation rates with operating time, *e.g.* due to chromia poisoning of mixed ionic electronic conducting (MIEC) solid oxide fuel cell cathodes or silica poisoning of gas sensors. In the literature most studies addressing long term stability aim to render the surface more robust against poisons, while others propose methods to limit poison exposure. In this study, we demonstrate not only the ability to recover the initial performance of a chromia-poisoned cathode material by subsequent infiltration with a Li-source binary oxide with high basicity, but enhance its performance (faster oxygen exchange kinetics and lower area specific resistance) above that of the pristine specimen. This study serves as a proof of concept, that through systematic control of the relative acidity of the surface, it is possible to regenerate poisoned metal oxide surfaces.

Introduction

The chemical degradation of surfaces due to both internal and external poisoning sources limits the long-term performance of metal oxides in a variety of application fields ranging from energy storage and conversion to sensors.[1–8] Degradation in performance is often associated with decreased oxygen surface exchange kinetics. Many studies have focused on optimizing the initial surface exchange kinetics, *e.g.* in solid oxide fuel and electrolysis cells (SOFCs/SOECs), permeation membranes and solar thermochemical reactors.[9–17] While the initial reactivity is important, maintaining performance over time is critical and often less examined. Today acceptable performance and degradation values (0.2–0.5% per 1000 h) are attained with single cells, but reliability and endurance must be increased in stacks where degradation rates are 2–4 times higher, due to *e.g.* Cr-poisons.[18] The US Department of Energy has set the ambitious

[a] *Department of Materials Science and Engineering, Massachusetts Institute of Technology, Cambridge, MA, 02139, USA. E-mail: tuller@mit.edu*
[b] *International Institute for Carbon-Neutral Energy Research (I²CNER), Kyushu University, Fukuoka, 819-0385, Japan*
[c] *Université de Nantes, CNRS, Institut des Matériaux Jean Rouxel, IMN, F-44000 Nantes, France*

† Electronic supplementary information (ESI) available. See DOI: https://doi.org/10.1039/d1ee03975j

‡ These authors contributed equally.

goal of reaching a stack voltage degradation rate target of 0.2%/1000 hours by 2035–2050.[18] Assuming degradation targets can be met, a global SOFC market size of $5.3 billion by 2028 is projected.[19] Identifying means for recovering the degraded performance of poisoned metal oxide electrodes would thus have great value in rendering this technology commercially viable.

As an example, in SOFCs and SOECs, mixed ionic electronic conducting (MIEC) perovskite oxides, such as (La,Sr)(Co,Fe)O_3 (LSCF), provide high oxygen surface exchange rates, making them efficient air electrodes.[20–25] While their initial performance is very promising, they remain susceptible to surface poisoning upon prolonged cell operation. Extensive non-active cation segregation, primarily Sr, to the electrode surface is well-documented as leading to blocking of the active surface with a charge transfer barrier (*e.g.* SrO layer) resulting in reduced reaction rates *e.g.* for the oxygen reduction reaction (ORR) in SOFCs.[26–29] Furthermore, segregated SrO has been found to be a preferred nucleation site for chromium species, resulting in the formation of $SrCrO_4$.[30] Chromium is well known to be the most pervasive extrinsic surface poison for SOFCs and is inherent to the operation of fuel cell stacks.[31–35] Ferritic steels with a chromium content between 18 and 25% are well suited interconnect materials, given their need to be simultaneously electronically conducting, oxidation resistant, impermeable to gas diffusion, stable and compatible with the other fuel cell materials, as well as being inexpensive.[36] Unfortunately, Cr inevitably finds its way from the interconnect to the cathode during operation *via* vapor phase or surface diffusion. The vapor pressures of the various volatile chromium oxide sources including CrO_3(g), CrO_2(g), and CrO(g) over Cr_2O_3(s) increase with increasing oxygen partial pressure characteristic of the cathode environment. Additionally, the rate of degradation is increased in humidity attributed to $CrO_2(OH)_2$(g).[37,38] While barrier coatings (*e.g.* $(Mn,Cr)_3O_4$ spinel) have been applied to the Cr containing metal interconnects with the objective of reducing Cr volatility, they have not succeeded in completely mitigating long-term Cr induced cathode electrochemical degradation.[37]

In addition to limiting exposure to impurity sources, strategies to make air electrodes more robust through, *e.g.* the addition of getters,[1,39–43] and other surface modifications[40,44–46] have been investigated. Two notable examples are the work of Zhao *et al.* in which the addition of a thin La_2O_3 layer was found to recover, to a significant extent, the degradation in the oxygen exchange rate resulting from silica,[43] and Niu *et al.* who found enhanced tolerance of LSCF against Cr poisoning through infiltration with a multiphase additive.[42] In the latter case, the authors attribute the increased tolerance specifically to the $BaCO_3$ phase of the additive. In both cases the rationale for selecting the additive is based on empirical findings, *i.e.* the gettering ability of La_2O_3 or previous success with a multiphase additive. However, no comprehensive model was found in the literature that allows one to predict, *a priori*, the efficacy of additives in compensating degradation.

In our recent work, we showed that the Smith acidity scale for binary oxides can be used as a powerful descriptor for predicating their effect on the oxygen exchange coefficient (k_{chem}) of MIEC oxides.[47] As a result, infiltration with binary oxides, ranging from strongly basic (Li_2O) to strongly acidic (SiO_2), onto the surface of $Pr_{0.1}Ce_{0.9}O_{2-\delta}$ (PCO), a chemically stable fluorite, free of inherent poison sources (*e.g.* segregated Sr), systematically varied k_{chem} by over 6 orders of magnitude. Li_2O increased k_{chem} by nearly 1,000 times over that of pristine PCO, while SiO_2 depressed k_{chem} by nearly the same factor.[47] Interestingly, both Cr_2O_3 and SiO_2 were determined to be acidic by Smith,[48] suggesting that this feature could likely be the primary reason that these compounds serve to poison the ORR on SOFC cathodes.[47] With this insight, we hypothesized that not only could the Smith acidity be used to determine the influence of a single additive, but that the surface exchange kinetics could be tuned by adding multiple infiltrants and thereby controlling the relative surface acidity. In this study, we systematically examine the effect of serial infiltration of acidic and basic oxides on the exchange coefficient using electrical conductivity relaxation experiments on porous PCO bulk specimens. Indeed, we found that serial infiltration with Li_2O compensates the initial degradation caused by acidic Cr_2O_3, resulting in even better performance than pristine PCO. We further verified the relevance of these findings by examining changes in area-specific resistance (ASR) associated with the oxygen exchange reaction in a symmetric cell and gained insight into the surface additive chemistry using microscopy. In addition to the importance of predicting and optimizing SOFC cathode performance and durability, this same concept can be applied to other applications in which extrinsic surface poisoning limits long-term operation, *e.g.* electrolyzers, oxygen permeation membranes and gas sensors.[1–8]

Results and discussion

Here we study how the addition of a basic infiltrate affects surface oxygen exchange kinetics degraded by Cr poisoning. The electrical conductivity of mixed conducting oxides varies with oxygen stoichiometry *i.e.* with variation in the surrounding oxygen partial pressure. By monitoring the electrical conductivity transient after a rapid step change in oxygen partial pressure, the kinetics associated with the uptake or release of oxygen by the oxide can be determined.[49] There are a number of factors to consider in insuring the correct interpretation of electrical conductivity relaxation measurements in porous specimens. One must ensure that neither gas phase diffusion inside the pores nor bulk oxygen diffusion within the solid materially impact the kinetics, but rather that only the surface oxygen exchange kinetics are limiting.[50,51] In our preceding study,[47] we verified that the overall kinetics of the prepared porous PCO specimen are not limited by gas phase diffusion inside the pores under the measurement conditions (see Supplementary Note 1-1, Table S1 and Fig. S1, S2 in the ESI†). While the oxygen equilibration kinetics in general depend on both bulk oxygen diffusivity and the surface exchange reaction, by selecting a microstructure characterized by a physical oxygen

diffusion length (~1 μm based on grain size) much shorter than the critical thickness of PCO (3.6×10^3 μm at 670 °C,[52] above which bulk oxygen diffusion becomes dominant), readily ensures that the reduction/oxidation kinetics are solely determined by surface oxygen exchange, consistent with the report by M.W. Den Otter *et al.*[50] (see Supplementary Note 1-2 in the ESI†). Thus, a porous specimen of PCO with a grain size of approximately 1 μm, and a geometrically determined porosity of 26%, was selected to ensure surface limited oxygen exchange kinetics. An additional benefit of this measurement is that the surface can be easily infiltrated with ethanol-based solutions of $Cr(NO_3)_3$ and $LiNO_3$. The nitrates fully decompose following *in situ* calcination in synthetic air at 600 °C. The PCO specimen is measured once, prior to infiltration, to provide a reference data set of k_{chem}. Then, the specimen is infiltrated with chromium, starting with low loading (0.02 at% with respect to PCO) and re-measured. In order to determine the dependence of the degradation level on Cr-concentration, the infiltration was repeated three times to increase Cr loading incrementally (up to 0.3 at%). The sample was re-measured by conductivity relaxation following each subsequent infiltration. In an attempt to reactivate the exchange rate of oxygen, the same porous PCO specimen was then infiltrated a total of four additional times (up to 0.5 at%) with Li-species and re-measured after each infiltration step. A schematic illustrating the sequence of infiltrations of Cr- and Li-based nitrate solutions into the porous PCO specimen is shown in Fig. 1a, with the infiltration notation used hereafter described as the sum of the infiltration amount. In the low resolution scanning electron microscopy (SEM) images, no significant microstructural change of the PCO specimen was observed following all seven infiltration steps; compare Fig. 1b–d. In order to gain more detailed chemical information about surface chemistry and to examine the structure of the additives, scanning transmission electron microscopy with electron energy loss spectroscopy (STEM-EELS) was used. The energy loss near-edge fine structure (ELNES) is based on the number of unoccupied states and highly dependent on the local chemical environment that

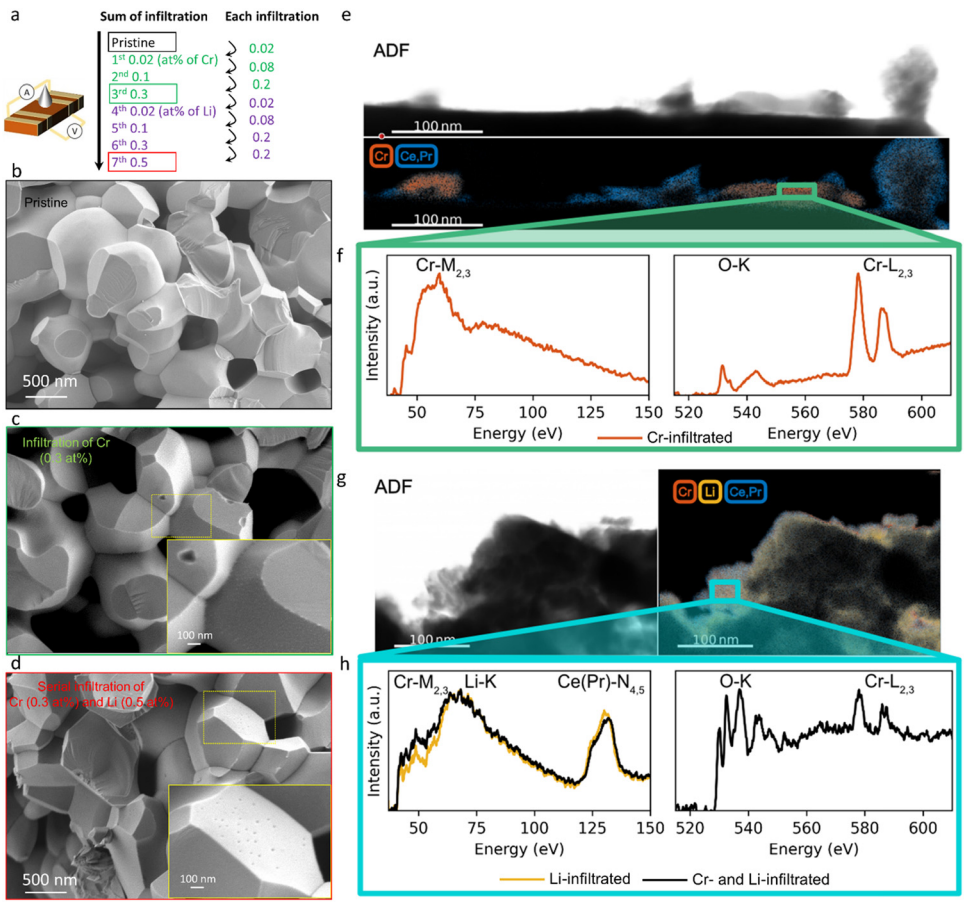

Fig. 1 (a) Schematic of procedure to sequentially infiltrate Cr- and Li-based nitrate solutions into $Pr_{0.1}Ce_{0.9}O_{2-\delta}$ (PCO) porous specimen, electrode to enable conductivity relaxation measurements, following step changes in pO_2. Each infiltration level and the subsequent sum of infiltration levels are illustrated. Cross-sectional SEM images of (b) pristine PCO porous specimen and (c) following third serially infiltrated step of Cr and (d) following forth serially infiltrated step of Li. (e) Annular dark field (ADF) image (top) and Electron Energy Loss Spectroscopy (EELS) elemental mapping of Cr-$M_{2,3}$ and Ce(Pr)-$N_{4,5}$ edge in Cr-infiltrated PCO (bottom). (f) EELS spectra around Cr-$M_{2,3}$ (left), and O-K and Cr-$L_{2,3}$ (right) edge in Cr-infiltrated PCO. (g) ADF image (left) and EELS elemental mapping of Cr-$M_{2,3}$, Ce(Pr)-$N_{4,5}$, and Li-K edge in serially Cr- and Li-infiltrated PCO specimen (right). (h) EELS spectra of Cr-$M_{2,3}$/Li-K in serially Cr- and Li-infiltrated PCO specimen (black) and of Li-K edge in pure Li-infiltrated PCO (yellow) in the left panel. Right panel shows the O-K and Cr-$L_{2,3}$ edge of serially Cr- and Li-infiltrated PCO specimen.

creates a unique ''fingerprint'' for each element and phase that is used to determine the spatial distribution of atomic species.[53] Fig. 1e (Fig. S3a, ESI†) presents an image of the 0.3 at% Cr-infiltrated PCO surface. The top panel shows the annular dark field (ADF) image and bottom the elemental mapping of Cr-rich regions in red and PCO regions in blue. The spectra for the Cr-$M_{2,3}$ and O-K and Cr-$L_{2,3}$ edges are shown in Fig. 1f. Based on the EELS white-line ratios between Cr-L_2 and Cr-L_3 the Cr-rich regions are crystalline Cr_2O_3 (alpha).[54] This indicates, in line with the SEM image (see Fig. 1c), that the infiltration forms tens of nm scale Cr_2O_3 crystallites on the surface of PCO. In the case of perovskite electrodes, in addition to the formation of Cr_2O_3 crystallites, authors often report the formation of chromates with intrinsic poisons, *e.g.* segregated Sr on the surface. For more information see the comprehensive review by Jiang *et al.*[3] Given that PCO is free of intrinsic poison sources, such products are not expected here.

In the images of the 0.3 at% Li-infiltrated PCO surface, no crystalline Li_2O phase is visible. Instead, the Li-species are finely dispersed on the PCO surface. These spectra taken of the pure Cr- and Li-infiltrated PCO specimens will be used as a reference for the serial Cr- and Li-infiltrated samples. Fig. 1g shows the ADF image (top) and elemental mapping of Li-K, Cr-$M_{2,3}$, and Ce(Pr)-$N_{4,5}$ edges in yellow, red and blue, respectively (bottom). Similar to the pure Li-infiltrated sample, we find the infiltrated species are uniformly distributed on PCO in the serial infiltrated samples (Fig. 1g and Fig. S3b, ESI†). Although the presence of Cr can be confirmed by the Cr-$L_{2,3}$ edge intensities in the right panel of Fig. 1h, there are no regions with only Cr-species (Fig. S3c, ESI†). Instead, the Cr signal is accompanied by those for Li, Ce and Pr, and therefore greatly reduced in intensity. This finding, and the changes in the white-line ratio in the serial infiltrated PCO compared to the Cr-infiltrated PCO (Fig. 1f and h) from the EELS spectra, suggest that crystalline Cr_2O_3 reacts with the Li-species forming mixed amorphous phases composed of Cr, Li, Ce, Pr and O. Based on the STEM observations, the Li-species chemically react with the surface oxide and dissolve both Cr_2O_3 and PCO into an amorphous mixed oxide. This process is likely driven by the strong reactivity of Li with ceria, consistent with the reported use of Li_2O as a sintering aid in the densification of ceria.[55,56]

Conductivity relaxation experiments were used to extract the oxygen chemical surface exchange coefficients k_{chem} of both the pristine PCO specimen and those serially infiltrated with Cr- and Li-species. Fig. 2a presents the normalized transient conductivity response to a step change in oxygen partial pressure from 0.1 atm to 0.2 atm of the pristine, Cr- and subsequently Li-infiltrated PCO specimen measured at 400 °C. The oxygen exchange coefficient, k_{chem}, was calculated by fitting the conductivity transients with the following equation:

$$g(t) = \frac{\sigma(t) - \sigma_0}{\sigma_\infty - \sigma_0} = 1 - \exp\left(-k_{chem}\frac{A}{V}t\right) = 1 - \exp\left(-\frac{t}{\tau}\right) \quad (1)$$

where $\sigma(t)$, σ_0, and σ_∞ are the electrical conductivity at time t, at the initiation of the step in pO_2 and at infinite time, and τ is the time constant of the transient, respectively. The geometrical factor A/V corresponds to the surface area to volume ratio of the solid phase. The detailed fitting procedure is described in Supplementary Note 2-1 in the ESI.† As for the pristine specimen, those infiltrated with Cr exhibited a transient profile characterized by a single time constant exponential. The detailed fitting process utilized in analyzing the conductivity transients of the Cr-infiltrated specimens with concentrations above 0.02 at% concentrations can be found in Supplementary Note 2-2 and Fig. S5a–d in the ESI.† First, the Cr loading was gradually increased from 0.02 to 0.3 at%. The same porous specimen was then infiltrated with increasing levels of the basic Li additive from 0.02 up to 0.5 at%. However, beginning with the Li-infiltration concentration of 0.1 at%, the conductivity transients changed to two time constant exponentials. The resulting k_{chem} values were extracted utilizing an average time constant. The fitting results with two time constants are described in Supplementary Note 2-3, Fig. S5f–h and Table S2 in the ESI.†

An Arrhenius plot of the k_{chem} values extracted by fitting the normalized conductivity transient profiles at a series of temperatures is presented in Fig. 2b. The initial 0.02 at% Cr-infiltration already substantially impedes the rate of response to the step change in pO_2. Additional Cr-infiltration further degrades the exchange kinetics. Above 0.1 at%, the sample appears saturated, as further loading with 0.3 at% does not lead to further decreases in k_{chem} (Fig. 2b and c). Subsequent low concentration Li-infiltration (0.02 at%) leads to little change in k_{chem} values. At higher concentrations, however, significant recovery in exchange rate was observed. For Li-infiltration at levels of 0.3 and 0.5 at%, the relaxation becomes too rapid, in the same temperature regime (400–600 °C), to enable the evaluation of k_{chem} values from the transient response, given that the time constants drop below the flush time limit of the reactor. They could, however, be determined by repeating the transient studies at lower temperatures, and then extrapolating to 400 °C for comparison. This explains why different temperature windows for the various samples, presented in Fig. 2b, were employed.

The exchange kinetics exhibit an extremely strong dependence on the serial Cr- and Li-infiltration sequence, with k_{chem} values varying by more than three orders of magnitude between Cr-species (0.1 at%) and Li-species (0.5 at%). Cr-infiltration at the 0.1 at% level resulted in a roughly 20-fold decrease in k_{chem} as compared to pristine PCO, while serial Li-infiltration of 0.5 at% led to a boost in k_{chem} by >1000 fold, more than fully recovering the initial value of the pristine PCO specimen, as shown in Fig. 2b and c. Although measurements were repeated seven times following serial Cr- and Li-infiltrations, the activation energy (E_a) of k_{chem} showed little dependence on infiltration, in contrast to the very dramatic changes in magnitude observed for k_{chem} (Fig. 2c and Fig. S6, ESI†), consistent with similar observations in our earlier study that was limited to infiltration of individual binary oxides with controlled acidity into PCO.[47] The relatively larger error bars in the activation energy may be connected to the increasing co-existence of

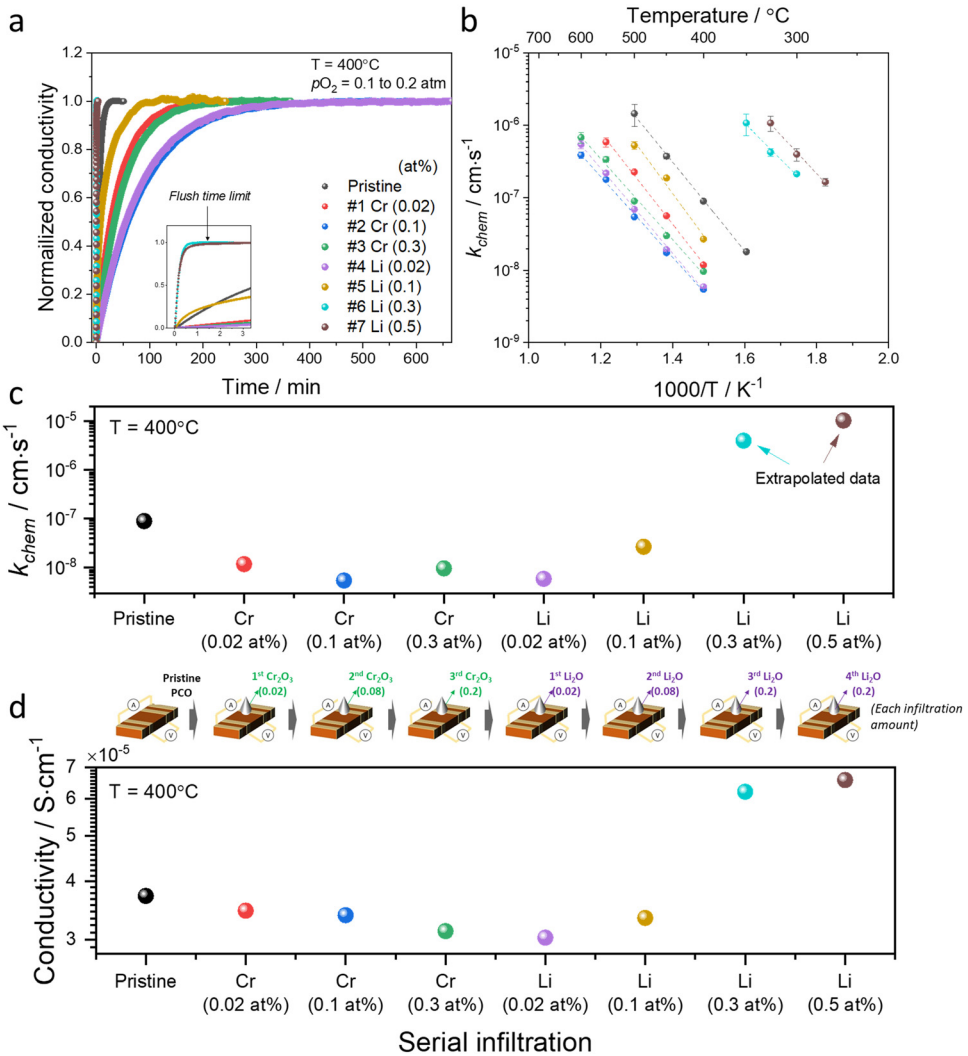

Fig. 2 (a) Normalized conductivity relaxation profile in response to pO_2 step (0.1 to 0.2 atm) beginning with a pristine PCO specimen and following successive Cr- and Li-infiltration, measured at 400 °C. (b) Arrhenius plot of log surface oxygen exchange coefficient (k_{chem}) *vs.* reciprocal temperature. Error bars in (b) were derived from fitting transient profiles with and without the flush time correction, see Supplementary Note 1-1 (ESI†). Comparison of (c) k_{chem} and (d) conductivity values obtained at 400 °C of pristine PCO followed by subsequent Cr- and Li-infiltrations, respectively. Inset of illustration between (c) and (d) shows the concentrations associated with the serial infiltrations of Cr (from 0.02 to 0.3 at%) and then Li (0.02 to 0.5 at%). The cartoon between (c) and (d) indicates each infiltration amount.

mixed Cr-rich and Li-rich regions, with some varying distributions in these mixed regions. Notwithstanding these observations, there is no obvious trend in activation energy with infiltration of either Cr- or Li-species.

In concert with our earlier findings,[47] we also found that the overall electrical conductivity (σ) of the PCO specimens was impacted by infiltration with the steady state conductivity decreasing upon acidic Cr-infiltration, while increasing under subsequent basic Li-infiltration. Fig. 2d shows that acidic 0.3 at% Cr-infiltration decreased the conductivity values of PCO by 19% at 400 °C, while a 117% improvement of the poisoned specimen's conductivity was observed following serial Li-infiltration at 0.5 at%. Note the correlation between the trend in k_{chem} with that of conductivity (Fig. 2c and d). Although the conductivity changes show a similar tendency, percent changes in conductivity are much lower than those for k_{chem}. This is not surprising given that any accumulation or depletion of electrons induced by additives should only affect the near-surface conductivity of PCO, and not the bulk as a whole. Thus, the smaller changes in overall conductivity are expected and are in line with the previously reported results.[47] The dramatic changes of several orders of magnitude in k_{chem} that are directly controlled by the surface can also be interpreted. Acidic Cr-species result in surface electron depletion, while basic Li-species lead to surface electron accumulation, in turn decreasing or increasing the conductivity of PCO upon serial infiltration. Previously, we attributed the reduction/enhancement of k_{chem} to the depletion/accumulation of surface electrons that facilitate oxygen exchange[47,57] With this insight, it is now possible to argue that the ability of additives to mitigate the poisoning behavior of acidic oxides can be predicted using the Smith acidity descriptor.

All specimens exhibited similar E_a values for the electrical conductivity (taken from the in-plane resistance measurements) of approximately 1.1–1.2 eV for temperatures between 500 °C and 350 °C (Fig. S7, ESI†) except for those with high levels of Li-infiltration that show a lower value of approximately 0.9 eV. In this temperature and pO_2 range, the electronic conductivity σ_e is given by:[58–60]

$$\sigma_e = nq\mu_e = \left(K^{\circ}_{r,Pr}\exp\left(\frac{-H_{r,Pr}}{3k_BT}\right)\right) \times pO_2^{-\frac{1}{6}} q\frac{\mu^{\circ}_{Pr}}{T}\exp\left(\frac{-H_{m,Pr}}{k_BT}\right) \quad (2)$$

where n is the electron density, q the charge of the electron, μ_e the electron mobility, $H_{m,Pr}$ the electron small polaron hopping energy, $K^{\circ}_{r,Pr}$ the prefactor of the PCO reduction reaction, $H_{r,Pr}$ the reduction enthalpy, pO_2 the oxygen partial pressure, k_B & T taking on their normal meanings. The obtained activation energy values match well with the sum of the electron small polaron hopping energy ($H_{r,Pr}$ = 0.56 eV) and one third of the reduction enthalpy $\left(\frac{H_{r,Pr}}{3} = 0.63\,eV\right)$ that together equal 1.19 eV.[58] The dominant conduction pathway is *via* small polaron hopping in the Pr 4f band. Acidic Cr-species deplete the electrons from this Pr 4f band, decreasing the conductivity without affecting the activation energy. Interestingly, for high Li-loadings, not only does the conductivity increase, but the activation energy is approximately 0.2 eV lower than in pristine PCO. In their theoretical work on PCO, Elm *et al.* conclude that following full reduction of Pr(IV) to Pr(III), the next state to become occupied is the higher lying Ce(4f)-state.[61] Following electron transfer from Li containing species to the PCO surface, and subsequent electron accumulation, the near surface Pr 4f levels are expected to become fully occupied, leading to occupation of the higher lying Ce 4f levels. Given the lower reported activation energy associated with small polaron hopping *via* the Ce 4f band of 0.39 eV,[59] this would explain the reduction in overall activation of conduction by ~0.17 eV. On the other hand, the reduction enthalpy of PCO is a bulk characteristic and therefore should not be expected to vary with surface infiltration.

Our conductivity relaxation measurements in this, and in our previous study,[47] show a clear inverse correlation between the relative acidity of the infiltrated oxides and the oxygen exchange reaction rate, k_{chem}. In an electrochemical cell, the polarization resistance of the cathode (*i.e.* area-specific resistance, ASR) reflects contributions from a number of sources including the oxygen exchange kinetics, gas diffusion limitations, contact resistance, effective in-plane conductivity, and ion transfer processes across the electrolyte–cathode interfaces.[62–66] The fraction of the ASR responsible for the oxygen exchange kinetic limitations, which we define by R_S, should follow the inverse relationship to k_{el} given by:

$$k_{el} = \frac{k_BT}{4e^2R_Sc_O} \quad (3)$$

where k_B is the Boltzmann constant, T the temperature in Kelvin, and c_O the total concentration of lattice oxygen (5.035×10^{22} cm^{-3},[52]). k_{el} differs from k_{chem} as they are derived from experiments that use different driving forces, namely electrical potential (impedance spectroscopy) *vs.* chemical potential (pO_2 step in conductivity relaxation) gradients. To compare the chemically- and electrically-driven oxygen exchange reaction coefficient values from the conductivity relaxation and electrochemical impedance measurements, respectively, the thermodynamic factor (w_e) and surface area (S_A) should be considered. Accordingly, the values of electrical oxygen exchange coefficient (k_{el}) were converted to k_{chem} with the aid of the following equation,[67]

$$k_{chem} \times S_A = k_{el} \times w_e = \frac{k_BT}{4e^2R_Sc_O} \times w_e \quad (4)$$

To test if this relationship between k_{chem} and R_S holds true here as well, the ASR of pristine and infiltrated PCO electrodes were examined using electrochemical impedance spectroscopy (EIS). Symmetrical cells with two nominally identical PCO electrodes, screen printed onto both sides of an YSZ single-crystal substrate were used (Fig. 3a). Similar to the procedure followed in the conductivity relaxation measurements, a reference PCO symmetric cell was first characterized by impedance spectroscopy, and then again after successive infiltration with Cr (0.15 at%) and subsequently Li (0.4 at%). To ensure the ability to reactivate a Cr-poisoned cell even after exposure to high Cr concentrations, 0.15 at% Cr-species (over four times the concentrations found by Menzler *et al.* after 3000 hours of stack operation[68]) were added to each side of a symmetric cell. Impedance spectra were fitted with three serial R–Q circuit elements (inset in Fig. 3b). The total ASR (sum of $R2$, $R3$ and $R4$) obtained from Nyquist plots at 575 °C (Fig. 3b) increased nearly nine-fold as a result of the Cr-infiltration. Reactivation of a cell initially infiltrated with Cr-species by subsequent Li-infiltration (0.4 at%) resulted in more than a 22-fold decrease in total ASR below its initial value. The Nyquist plots of the impedance spectra, however, are distorted as a result of several overlapping processes in the frequency regime of interest. In order to better differentiate the different sources of losses in the cell, the distribution of relaxation times (DRT) approach was utilized in which the characteristic peaks can be more readily distinguished as observed in Fig. 3c.[69–71] Using the DRT method shows that the infiltration significantly affects the lower frequency peak ($P1$), which correlates to $R4$. $R2$ and $R3$ show little dependence on infiltration (Fig. S8, ESI†) and are likely associated with ion transfer processes across the electrolyte–cathode interface.[64,65] These losses will therefore not be examined in further detail. Only $R4$ exhibits a strong dependence on infiltration, changing by orders of magnitude. In this frequency region, the losses are commonly attributed to surface oxygen exchange processes including oxygen adsorption and dissociation, as well as mass transfer processes *i.e.*, gas diffusion within the cathode pores.[65,66] The resistance of $P1$ obtained from DRT, determined *via* peak fitting, is however thermally activated (thus not controlled by gas diffusion). One can correlate $R4$

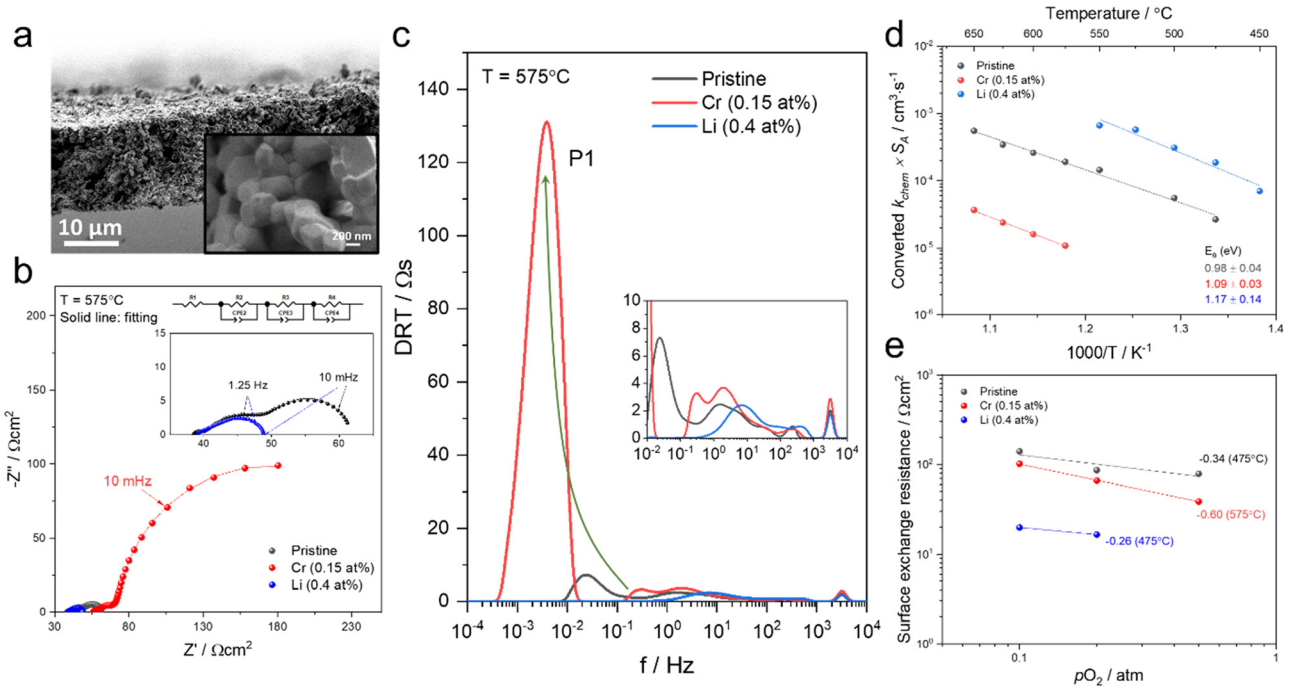

Fig. 3 (a) SEM image of screen printed PCO electrode/electrolyte interface in prepared PCO/YSZ/PCO symmetric cell at two levels of magnification. (b) Nyquist plots and (c) distribution of relaxation time (DRT) plots of the pristine, Cr-infiltrated, and Cr- and Li-infiltrated symmetric cells obtained at 575 °C with pO_2 = 0.1 atm. Three serial R–Q circuit elements were used. (d) Temperature dependence of converted $k_{chem} \times S_A$ by using eqn (4) based on extraction of the surface exchange resistance and (e) pO_2 dependence of the surface exchange resistance obtained from fitting the Nyquist plot.

and the resistance associated with *P*1, given that both exhibit similar magnitudes and activation energies (here only the detailed evaluation of *R*4 is included (for analog evaluation of *P*1 see Fig. S9, ESI†). *R*4 values were converted to $k_{chem} \times S_A$ with the aid of eqn (4). As S_A is not trivial to determine, but should remain largely constant between the samples, it is considered an arbitrary constant that does not influence E_a. In Fig. 3d, we observe that the activation energies of 1.0–1.2 eV, match well with those obtained for k_{chem}, further indicating that *R*4 reflects losses directly associated with the oxygen exchange processes. Based on the thermal activation and relatively high pO_2 power law dependence (*ca.* 0.34) (Fig. 3e), which is consistent with the previously reported values (ranging from −0.3 to −0.7), we attribute *R4* to oxygen exchange processes (R_s) on the PCO surface.[47,52,67,72–74] For the pristine cell, and after the serial Li-infiltration, it was difficult to clearly discern the surface oxygen exchange resistance (R_s) at high temperatures and high pO_2. In these cases, the oxygen dependence, was therefore determined at 475 °C. The surface exchange resistance increases by a factor of almost 20 upon Cr-infiltration and shifts to lower frequencies. Interestingly, after the serial Li-infiltration, R_s significantly decreases by over two orders of magnitude (see Fig. 3d and Fig. S9 in the ESI†).

The corresponding capacitance (*C*4) was calculated by fitting results from the Nyquist plot. The resulting high *C*4 values of the cells at 575 °C (for Li-infiltration at 475 °C) fall in the range of 200 and 600 F cm^{-3} and exhibit −1/6 slope dependence of log *C*4 on log pO_2 (Fig. S10, ESI†), which are in line with those previously reported for the chemical capacitance of PCO thin films,[75] further confirming that *C*4 corresponds to surface oxygen exchange processes that dominate R_s (see eqn (3)). Given that the chemical capacitance is associated with the volumetric characteristic of the electrode, we do not expect it to change dramatically with infiltration, while the surface exchange resistance does. The rate-determining step on the PCO surface remains under debate in the literature[47,57,72] and based on the findings in this work, it is not possible to draw a concrete mechanism for the detailed rate-determining step (*e.g.* oxygen adsorption, diffusion, charge transfer). Nonetheless, it is noteworthy that infiltrants strongly impact the surface oxygen exchange reaction.

Discussion and conclusions

Comparing the pristine, Cr-infiltrated and serially Cr-/Li-infiltrated samples using microscopy analysis, conductivity relaxation and electrochemical impedance measurements provides important insights into the mechanism responsible for the remarkable compensation of Cr-species by Li-species. As expected from our earlier study,[47] acidic Cr-infiltration decreases the oxygen surface reaction rate of PCO. Although in the STEM-EELS results, relatively large (tens of nm) Cr_2O_3 crystallite form, leaving a substantial amount of PCO surface free of readily visible Cr-species (although highly dispersed species are likely[47]), the oxygen exchange coefficient (by a factor of 20) and overall conductivity (by 19%) decrease significantly for 0.3 at% Cr. Moreover, Cr-infiltration severely degrades the

surface exchange resistance ($R4$ increases 20 times with 0.15 at%). Regardless of these large changes, the corresponding activation energies remain unchanged. Based on this finding and those of the previous report,[47] we attribute the degradation to the depletion of surface electrons in PCO as a result of the hetero-junction with Cr_2O_3. Through the serial Li-infiltration, it is not only possible to regenerate the oxygen surface reaction rate, but enhance it above that of the untreated PCO surface. The oxygen exchange rate (by a factor of 1000) and overall conductivity (by 117%) increase for 0.5 at% Li, while the surface exchange resistance decreases over 100 fold with 0.4 at% Li. After serial infiltration of Li, no crystalline lithia phase was observed, and crystalline Cr_2O_3 was no longer visible in the STEM-EELS results. Although no crystalline lithia phase remains, the Li-rich amorphous phase apparently retains its basicity, as indicated by its ability to recover rapid oxygen exchange rates. This hypothesis is further supported by the observations in Fig. 2d of increased conductivity of PCO when serial-infiltrated with Li-species, suggestive of electron transfer from the amorphous phase to PCO. The decomposition of the crystalline Cr_2O_3 phase, and its incorporation into an amorphous Li-rich phase, likely enhances the ability of the Li-infiltrate to more readily compensate for the chromia acidity and contribute to the regeneration of the oxygen exchange rate. Taken together, the positive impact of Li-infiltration on the exchange kinetics appears to originate from two features: (1) recovering the fraction of the PCO surface poisoned by Cr_2O_3 due to Li-induced decomposition of Cr_2O_3 and (2) increasing the overall surface electron concentration which facilitates oxygen exchange.

The ability to tune the oxygen exchange kinetics of metal oxides through the addition of surface additives, utilizing relative acidity as a guide, is demonstrated to be a powerful tool. This work serves as a proof of concept that the performance degradation of a mixed conducting oxide (PCO) induced by acidic poisons *e.g.* chromia, can be compensated through the serial addition of basic additives *e.g.* lithia. Strikingly, even using chromia concentrations over 10 times higher than expected after 3000 hours of stack operation, not only does one achieve the complete regeneration of the oxygen exchange kinetics through Li-infiltration, but also improvements above those found in the pristine sample. These findings are not only significant for insuring extended operation of SOFCs with reduced performance degradation rates, but for all applications where the oxygen exchange reaction at metal oxide surfaces plays a central role *e.g.* electrolyzers, oxygen permeation membranes and gas sensors. It thus offers insight into how the operation lifetimes of a variety of devices can be extended through the compensation of acidic poisons in general.

Author contributions

H. G. S., C. N. and H. L. T. conceived the original ideas. H. G. S., A. S., C. N. and H. L. T. designed the experimental protocol. H. G. S. prepared the porous structure specimen, built the experimental set-up, examined the microstructures and performed the conductivity relaxation measurements. A. S. prepared the PCO symmetric cells and performed the electrochemical impedance spectroscopy measurements. D. S. K. performed the STEM-EELS analysis with assistance of M. X. D. K. assisted in the interpretation of DRT and C. N. proposed the modeling of the electrical conductivity relaxation results. J. M. L. interpreted the STEM-EELS results. H. L. T. supervised the work and provided guidance throughout the project. H. G. S., A. S. and H. L. T. wrote the manuscript with inputs from all the co-authors. All the co-authors contributed to discussing the results and helped to revise the manuscript.

Conflicts of interest

There are no conflicts to declare.

Acknowledgements

This research was initially supported by the US Department of Energy (DOE), National Energy Technology Laboratory (NETL), Office of Fossil Energy under Award No. DE-FE0031668—Robust highly durable solid oxide fuel cell cathodes – Improved materials compatibility & self-regulating surface chemistry. Additional funding included support in part for H. G. S by the Basic Science Research Program through the National Research Foundation of Korea (NRF) funded by the Ministry of Education (No. 2021R1A6A3A03044464) and for H. G. S, A. S. and H. L. T with funds provided by the MIT Department of Materials Science and Engineering *via* the R. P. Simmons Professor of Ceramics and Electronic Materials Chair. D. S. K., M. X. and J. M. L. acknowledge support for STEM characterization from the Air Force Office of Scientific Research (FA9550-20-0066).

References

1 M. Reisert, A. Aphale and P. Singh, *Materials.*, 2018, **11**, 2169.
2 M. Lankin, Y. Du and C. Finnerty, *J. Fuel Cell Sci. Technol.*, 2011, **8**, 1–7.
3 S. P. Jiang and X. Chen, *Int. J. Hydrogen Energy*, 2014, **39**, 505–531.
4 M. Schüler, T. Sauerwald and A. Schütze, *J. Sens. Sens. Syst.*, 2015, **4**, 305–311.
5 D. E. Williams and K. F. E. Pratt, *J. Chem. Soc., Faraday Trans.*, 1998, **94**, 3493–3500.
6 M. van Essen, P. Visser, S. Gersen and H. Levinsky, *SAE Int. J. Fuels Lubr.*, 2018, **11**, 35–42.
7 M. M. Viitanen, R. G. V. Welzenis, H. H. Brongersma and F. P. F. Van Berkel, *Solid State Ionics*, 2002, **150**, 223–228.
8 B. W. Holleboom, S. W. Hawes and E. L. Ker, *SAE Tech. Pap. Ser., Technical Paper 860478*, 1986.
9 A. Steinfeld, *Sol. Energy*, 2005, **78**, 603–615.
10 W. C. Chueh, C. Falter, M. Abbott, D. Scipio, P. Furler, S. M. Haile and A. Steinfeld, *Science*, 2010, **330**, 1797–1801.

11 J. Sunarso, S. S. Hashim, N. Zhu and W. Zhou, *Prog. Energy Combust. Sci.*, 2017, **61**, 57–77.
12 C. Graves, S. D. Ebbesen, S. H. Jensen, S. B. Simonsen and M. B. Mogensen, *Nat. Mater.*, 2015, **14**, 239–244.
13 S. Y. Gómez and D. Hotza, *Renewable Sustainable Energy Rev.*, 2016, **61**, 155–174.
14 M. A. Laguna-Bercero, *J. Power Sources*, 2012, **203**, 4–16.
15 J. H. Myung, D. Neagu, D. N. Miller and J. T. S. Irvine, *Nature*, 2016, **537**, 528–531.
16 J. Sunarso, S. Baumann, J. M. Serra, W. A. Meulenberg, S. Liu, Y. S. Lin and J. C. Diniz da Costa, *J. Membr. Sci.*, 2008, **320**, 13–41.
17 A. A. Plazaola, A. C. Labella, Y. Liu, N. B. Porras, D. A. P. Tanaka, M. V. S. Annaland and F. Gallucci, *Processes*, 2019, 7(3), 128.
18 S. D. Vora, U.S. DOE Office of Fossil Energy Solid Oxide Fuel Cell Program, 2018, Proceedings – 19TH Annual Solid Oxide Fuel Cell (Sofc) Project Review Meeting, **https://netl.doe.gov/node/7801**.
19 Fortune Bus. Insights, 2021, **https://www.fortunebusinessinsights.com/industry-reports/solid-oxide-fuel-cell-market-101306**.
20 J. A. Kilner and M. Burriel, *Annu. Rev. Mater. Res.*, 2014, **44**, 365–393.
21 A. Esquirol, N. P. Brandon, J. A. Kilner and M. Mogensen, *J. Electrochem. Soc.*, 2004, **151**, A1847.
22 J. Hwang, H. Lee, K. J. Yoon, H.-W. Lee, B.-K. Kim, J.-H. Lee and J.-W. Son, *J. Electrochem. Soc.*, 2012, **159**, F639–F643.
23 Z. Shao and S. M. Halle, *Nature*, 2004, **431**, 170–173.
24 Y. Chen, S. Yoo, Y. Choi, J. H. Kim, Y. Ding, K. Pei, R. Murphy, Y. Zhang, B. Zhao, W. Zhang, H. Chen, Y. Chen, W. Yuan, C. Yang and M. Liu, *Energy Environ. Sci.*, 2018, **11**, 2458–2466.
25 Y. Chen, Y. Bu, Y. Zhang, R. Yan, D. Ding, B. Zhao, S. Yoo, D. Dang, R. Hu, C. Yang and M. Liu, *Adv. Energy Mater.*, 2017, **7**, 1601890.
26 H. Tellez, J. Druce, Y. Shi, M. Kubicek, N. J. Simrick, J. L. M. Rupp, T. Ishihara and J. A. Kilner, *ECS Trans.*, 2015, **66**, 69–77.
27 W. Jung and H. L. Tuller, *Energy Environ. Sci.*, 2012, **5**, 5370–5378.
28 B. Koo, K. Kim, J. K. Kim, H. Kwon, J. W. Han and W. C. Jung, *Joule*, 2018, **2**, 1476–1499.
29 B. Koo, H. Kwon, Y. Kim, H. G. Seo, J. W. Han and W. Jung, *Energy Environ. Sci.*, 2018, **11**, 71–77.
30 S. P. Jiang and Y. Zhen, *Solid State Ionics*, 2008, **179**, 1459–1464.
31 S. P. S. Badwal, R. Deller, K. Foger, Y. Ramprakash and J. P. Zhang, *Solid State Ionics*, 1997, **99**, 297–310.
32 M. Kornely, N. H. Menzler, A. Weber and E. Ivers-Tiffée, *Fuel Cells*, 2013, **13**, 506–510.
33 A. Beez, K. Schiemann, N. H. Menzler and M. Bram, *Front. Energy Res.*, 2018, **6**, 1–8.
34 J. Tallgren, O. Himanen, M. Bianco, J. Mikkola, O. Thomann, M. Rautanen, J. Kiviaho and J. Van Herle, *Fuel Cells*, 2019, **19**, 570–577.
35 M. Bianco, J. P. Ouweltjes and J. Van herle, *Int. J. Hydrogen Energy*, 2019, **44**, 31406–31422.
36 J. G. Grolig, J. Froitzheim and J. E. Svensson, *J. Power Sources*, 2014, **248**, 1007–1013.
37 H. Kurokawa, C. P. Jacobson, L. C. DeJonghe and S. J. Visco, *Solid State Ionics*, 2007, **178**, 287–296.
38 R. Sachitanand, M. Sattari, J. E. Svensson and J. Froitzheim, *Int. J. Hydrogen Energy*, 2013, **38**, 15328–15334.
39 A. Aphale, J. Hong, B. Hu and P. Singh, *J. Visualized Exp.*, 2019, **147**, e59623.
40 K. Chen, N. Ai, K. M. O'Donnell and S. P. Jiang, *Phys. Chem. Chem. Phys.*, 2015, **17**, 4870–4874.
41 S. R. Bishop, J. Druce, J. A. Kilner, T. Ishihara and K. Sasaki, *ECS Trans.*, 2013, **57**, 2003–2007.
42 Y. Niu, Y. Zhou, W. Lv, Y. Chen, Y. Zhang, W. Zhang, Z. Luo, N. Kane, Y. Ding, L. Soule, Y. Liu, W. He and M. Liu, *Adv. Funct. Mater.*, 2021, **31**, 1–11.
43 L. Zhao, N. H. Perry, T. Daio, K. Sasaki and S. R. Bishop, *Chem. Mater.*, 2015, **27**, 3065–3070.
44 D. Ding, M. Liu, Z. Liu, X. Li, K. Blinn, X. Zhu and M. Liu, *Adv. Energy Mater.*, 2013, **3**, 1149–1154.
45 Y. Chen, S. Yoo, X. Li, D. Ding, K. Pei, D. Chen, Y. Ding, B. Zhao, R. Murphy, B. deGlee, J. Liu and M. Liu, *Nano Energy*, 2018, **47**, 474–480.
46 D. Ding, X. Li, S. Y. Lai, K. Gerdes and M. Liu, *Energy Environ. Sci.*, 2014, **7**, 552–575.
47 C. Nicollet, C. Toparli, G. F. Harrington, T. Defferriere, B. Yildiz and H. L. Tuller, *Nat. Catal.*, 2020, **3**, 913–920.
48 D. W. Smith, *J. Chem. Educ.*, 1987, **64**, 480–481.
49 C. B. Gopal and S. M. Haile, *J. Mater. Chem. A*, 2014, **2**, 2405–2417.
50 M. W. den Otter, H. J. M. Bouwmeester, B. A. Boukamp and H. Verweij, *J. Electrochem. Soc.*, 2001, **148**, J1.
51 Y. Zhang, F. Yan, B. Hu, C. Xia and M. Yan, *J. Mater. Chem. A*, 2020, **8**, 17442–17448.
52 D. Chen, S. R. Bishop and H. L. Tuller, *J. Electroceram.*, 2012, **28**, 62–69.
53 R. P. Ferrier, *Energy-Loss Spectroscopy in the Electron Microscope: Theoretical Considerations*, Springer, 3rd edn, 1981.
54 S. P. McBride and R. Brydson, *J. Mater. Sci.*, 2004, **39**, 6723–6734.
55 S. Le, S. Zhu, X. Zhu and K. Sun, *J. Power Sources*, 2013, **222**, 367–372.
56 C. Nicollet, J. Waxin, T. Dupeyron, A. Flura, J.-M. Heintz, J. P. Ouweltjes, P. Piccardo, A. Rougier, J.-C. Grenier and J.-M. Bassat, *J. Power Sources*, 2017, **372**, 157–165.
57 R. A. De Souza, *J. Mater. Chem. A*, 2017, **5**, 20334–20350.
58 D. Chen, A. Groß, D. C. Bono, J. Kita, R. Moos and H. L. Tuller, *Solid State Ionics*, 2014, **262**, 914–917.
59 S. R. Bishop, T. S. Stefanik and H. L. Tuller, *Phys. Chem. Chem. Phys.*, 2011, **13**, 10165–10173.
60 S. R. Bishop, T. S. Stefanik and H. L. Tuller, *J. Mater. Res.*, 2012, **27**, 2009–2016.
61 K. Michel, T. S. Bjørheim, T. Norby, J. Janek and M. T. Elm, *J. Phys. Chem. C*, 2020, **124**, 15831–15838.
62 S. B. Adler, *Chem. Rev.*, 2004, **104**, 4791–4844.
63 T. M. Huber, E. Navickas, K. Sasaki, B. Yildiz, H. Hutter, H. L. Tuller and J. Fleig, *J. Electrochem. Soc.*, 2018, **165**(9), F702–F709.
64 P. Caliandro, A. Nakajo, S. Diethelm and J. Van herle, *J. Power Sources*, 2019, **436**, 226838.

65 J. Hayd and E. Ivers-Tiffée, *J. Electrochem. Soc.*, 2013, **160**, F1197–F1206.
66 H. G. Seo, Y. Choi and W. C. Jung, *Adv. Energy Mater.*, 2018, **8**, 1–7.
67 J. J. Kim, *Defect Equilibria and Electrode Kinetics in $Pr_xCe_{1-x}O_{2-\delta}$ Mixed Conducting Thin Films: An in-situ Optical and Electrochemical Investigation, PhD thesis,* Massachusetts Institute of Technology, Cambridge, MA, 2015.
68 N. Menzler, F. Tietz, M. Bram, I. Vinke and L. Haart, in *Ceramic Engineering and Science Proceedings*, 2009, vol. 29, pp. 93–104.
69 E. Ivers-Tiffée and A. Weber, *J. Ceram. Soc. Japan*, 2017, **125**, 193–201.
70 T. H. Wan, M. Saccoccio, C. Chen and F. Ciucci, *Electrochim. Acta*, 2015, **184**, 483–499.
71 F. Ciucci and C. Chen, *Electrochim. Acta*, 2015, **167**, 439–454.
72 D. Chen, Z. Guan, D. Zhang, L. Trotochaud, E. Crumlin, S. Nemsak, H. Bluhm, H. L. Tuller and W. C. Chueh, *Nat. Catal.*, 2020, **3**, 116–124.
73 M. Schaube, R. Merkle and J. Maier, *J. Mater. Chem. A*, 2019, **7**, 21854–21866.
74 P. Simons, H.-I. Ji, T. C. Davenport and S. M. Haile, *J. Am. Ceram. Soc.*, 2017, **100**, 1161–1171.
75 D. Chen, S. R. Bishop and H. L. Tuller, *Adv. Funct. Mater.*, 2013, **23**, 2168–2174.